SCIENTIFIC REPORTS

OPEN

SUBJECT AREAS:
HYDROLOGY
OCEAN SCIENCES
ENVIRONMENTAL SCIENCES
PHYSICAL OCEANOGRAPHY

Received
12 June 2013

Accepted
21 May 2014

Published
17 June 2014

Correspondence and requests for materials should be addressed to X.-D.S. (xdshang@scsio.ac.cn)

Horizontal eddy energy flux in the world oceans diagnosed from altimetry data

Chi Xu[1], Xiao-Dong Shang[1] & Rui Xin Huang[2]

[1]State Key Laboratory of Tropical Oceanography, South China Sea Institute of Oceanology, Chinese Academy of Sciences, Guangzhou, China, 510301, [2]Woods Hole Oceanographic Institution, Woods Hole, MA 02543, USA.

During the propagation of coherent mesoscale eddies, they directly or indirectly induce many effects and interactions at different scales, implying eddies are actually serving as a kind of energy carrier or energy source for these eddy-related dynamic processes. To quantify this dynamically significant energy flow, the multi-year averaged horizontal eddy energy fluxes (EEFs) were estimated by using satellite altimetry data and a two-layer model based on hydrographic climatology. There is a strong net westward transport of eddy energy estimated at the mean value of ~13.3 GW north of 5°N and ~14.6 GW at the band 5°S ~ 44°S in the Southern Hemisphere. However, poleward of 44°S east-propagating eddies carry their energy eastward with an averaged net flux of ~3.2 GW. If confirmed, it would signify that geostrophic eddies not only contain the most of oceanic kinetic energy (KE), but also carry and spread a significant amount of energy with them.

Starting from the first international program, Mid-Ocean Dynamics Experiment and POLYMODE, aimed at observing mesoscale oceanic eddies[1] in 1970s, many programs, including early satellite altimetry missions such as SEASAT (1978) and GEOSAT (1986–1989) and the more recent altimetry missions Jason-2 and Envisat, demonstrate that the sea surface height (SSH) fields are full of mesoscale features[2,3]. Nearly synoptic global pictures of the eddy kinetic energy (EKE) distribution are now available from these advanced satellite altimetry missions[4–6]. Simple scale analysis[7] and altimetry data analysis[8, Plate 6] clearly show that EKE is two orders of magnitude larger than the mean flow KE. Ferrari and Wunsch[9] also concluded that "Oceanic KE is dominated by the geostrophic eddy field".

In addition, mesoscale eddies are the most significant and energetic component of ocean general circulation. They induce transport of heat, salt, carbon, and nutrients and interact with many other dynamic components at different spatial/temporal scales, such as atmospheric forcing[10], mean flow[11] and internal gravity waves[12]. They exert influence on inertial oscillations[13] and diapycnal mixing[14]. Moreover, the influence of eddies or isolated vortices can penetrate into the deep circulation[15–17].

Most mesoscale eddies move westward in basins with meridional boundaries, carrying energy westward[2,3]. However, up till now the quantified horizontal energy flux carried by eddies in the world oceans remains unclear. Because this is a critically important component of the global energy budget, a clear dynamical picture and a detailed balance are most desirable. Thus in this paper the eddy-related mechanical energy transport, including potential and kinetic energy (KE), was examined based on the previously published method[18].

Results

The eddy detection and auto-tracking (see Methods) based on weekly TOPEX/ERS merged sea surface height anomaly (SSHA) data over the period 1993 ~ 2010 were firstly conducted. Approximately 403,500 eddies were identified and the number of long-lived cyclonic (anticyclonic) eddies with lifetime ≥ 4 weeks were 72341 (67506); thus, 34.7% of the observed eddies were long-lived. As the derived eddy propagating speeds are able to significantly influence the final analysis, the results were compared with those derived from Chelton and Schlax dataset (http://cioss.coas.oregonstate.edu/eddies/, CS hereafter). As shown in Fig. 1, the results agree with theirs in latitudinal variations of both zonal averaged westward and zonal averaged northward propagating speeds. A map of the average values of the advective nonlinearity parameter defined by the maximum rotational current speed over the propagation speed of the eddy were also shown in Fig. 2 because strong nonlinearity means the energy will not radiate away at different scales but concentrate within the eddy[19].

Secondly, the eddy energy and associated energy source/sink were estimated by assuming that the water-column-integrated eddy kinetic energy (EKE) is equally partitioned between the barotropic mode and the first baroclinic mode and by using a two-layer model with equivalent interface depth inferred from a continuously

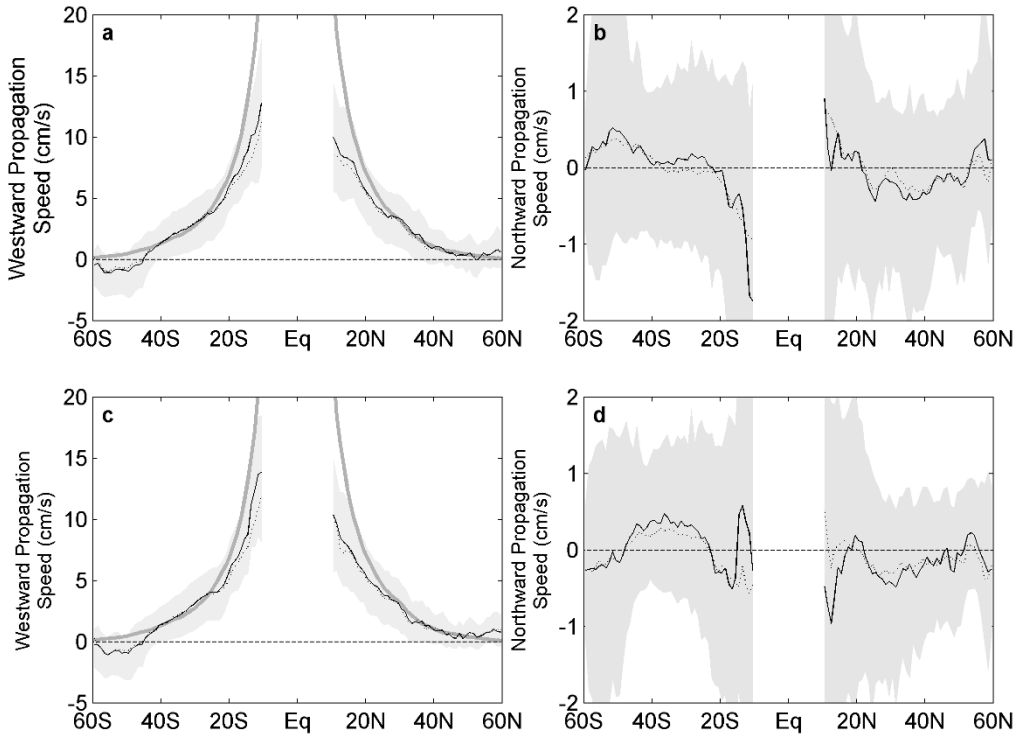

Figure 1 | The latitudinal profiles of the global zonal average of the westward (a), (c) and northward (b), (d) propagation speeds of cyclonic (a), (b) and anticyclonic (c), (d) eddies with lifetimes larger than 4 weeks, accumulated over 18 years. Results from our analysis are depicted by black solid lines with gray shading to indicate the interquartile range of the distribution of the eddy speeds in each 1° latitude band; while black dotted lines are based on the analysis of CS dataset. The gray solid lines in panels a & c are the latitudinal profile of the zonally averaged westward phase speeds of long baroclinic Rossby waves. MATLAB R2011a (http://www.mathworks.com/) was used to create the figure.

stratified model (see Method). The total amount of EKE is estimated at 0.96 EJ (1 EJ = 10^{18} J); the global amount of eddy available gravitational potential energy (EAGPE) is 1.63 EJ. The global distribution of eddy energy is shown in Fig. 3. It is found that the eastern part of the basin and the ocean interiors near the equatorial band (except the region where tropical instability waves exist) are characterized by the lower eddy energy, typically below the level of 10^3 J/m^2. The western part of basin, in particular the western boundary currents (WBCs, hereafter) and their extensions and the associated recirculation regimes, are characterized by rather high eddy energy (on the order of 10^4–10^5 J/m^2). Another outstanding feature is the high eddy energy, both EKE and EAGPE, associated with the Antarctic Circumpolar Current (ACC). These regions of high eddy energy are associated with energetic mesoscale variability due to strong baroclinic instability, and barotropic instability may also contribute to these regions of high eddy energy[20].

A map of eddy energy sources and sinks is shown in Fig. 4 (the color bar is chosen for best visualization). This map is rather similar to Figure 3 in ref. 21. Overall, dissipation of eddy energy is more dominating within the western boundary regions. Inferring from maps of mean eddy-energy generation rates and dissipation rates (Supplementary Fig. S1), intense eddy-energy dissipations and generations also occur in the ocean interior, in particular near the intense currents and the associated recirculation regimes. It means WBCs are also able to serve as a significant source of eddy energy. Based on this framework and the updated eddy searching scheme, the globally integrated eddy energy generation rates are estimated at 0.38 TW in EKE and 0.60 TW in EAGPE, with the total energy generation rate

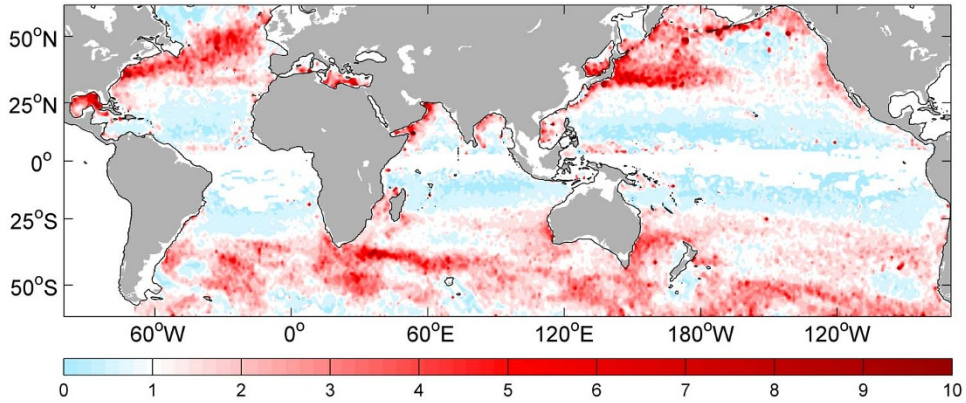

Figure 2 | The averaged values of U/c, where *U* is the rotational speed of an eddy and *c* is its translation speed at that moment. The rotational speed is defined here by the maximum of the averaged values of the geostrophic speeds around each closed SSHA contours of an eddy. The black thin line indicates the 200-m isobath. MATLAB R2011a (http://www.mathworks.com/) with M_Map (a mapping package, http://www.eos.ubc.ca/~rich/map.html) was used to create the map.

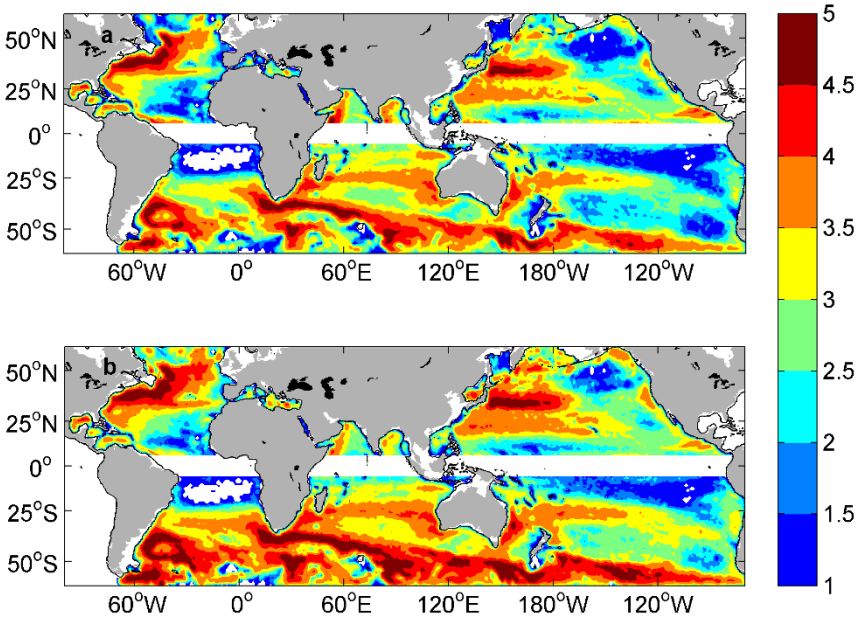

Figure 3 | Horizontal distribution of mean EKE (a) and mean EAGPE (b) in log10 form (of unit J/m²). The black thin line indicates the 200-m isobath. MATLAB R2011a (http://www.mathworks.com/) with M_Map (a mapping package, http://www.eos.ubc.ca/~rich/map.html) was used to create the map.

estimated at 0.98 TW. Both the volume of eddy energy and its generation rates are much larger than the value reported in the previous study. A comparison with estimates based on the cube92 version of the CS510 runs of the ECCO2 (Estimating the Circulation and Climate of the Ocean, phase II) and a discussion about the difference between this new estimate and other published results are included in the Supplementary Information.

Next step was to examine multi-year averaged horizontal eddy energy fluxes (EEFs, here after). With eddy energy and trajectory calculated, the zonal and meridional energy fluxes associated with moving eddies were calculated accordingly, Fig. 5.

Within the subtropical band, both cyclonic and anticyclonic eddies transport energy westward. Individual eddies are able to carry a large amount of energy, and the multi-year averaged EEF carried by these eddies can be as high as ~80 MW/degree westward. Due to the combination of high eddy concentration and high translation speed (as implicated by the formula of phase speed for the baroclinic first-mode Rossby waves), the westward EEF in the subtropical counter current around 20°N in the Pacific and in the subtropical gyres of the Southern Hemisphere around 25°S reach relatively high values. Cyclones and anticyclones give comparative contributions, except off the west coasts of Australia where EEF is dominated by cyclonic eddies[2,22].

Additionally, high EEF in WBCs and the recirculation systems are due to the strong unstable and meandering flows that give rise to shed-off eddies propagating within the recirculation systems. In the Northern Hemisphere around 35°N, especially on the equatorward side of the eastward currents like the Gulf Stream, the westward EEF carried by cyclones is able to reach the level of ~80 MW/degree (Fig. 5a). The circumstance on the equatorward side of the Kuroshio around 34°N is similar, but the corresponding EEF is much weaker. Likewise, the predominant energy flux induced by anticyclones appears on the poleward side of these eastward currents, but the regions are much narrower (Fig. 5c). This is consistent with the geographical distribution of eddy polarity discussed by ref. 2. In the Southern Hemisphere, along east coasts of continents strong westward components of EEF are associated with the strong WBCs, such as the Agulhas Current, the East Australian Current and the Brazil Current. Eddies in the Benguela Current contribute to another local high value of westward EEF.

Eastward EEF appears primarily in the ACC and other strong eastward boundary currents, such as the Kuroshio Extension at 38°N band, the Gulf Stream Extension at 40°N band and the Agulhas Return Current. The existence of eastward moving eddies may be explained by the fact that they are advected by mean flow[23]. The zonally averaged zonal EEF changes sign around 44°S (Fig. 6a). In particular, the latitudinal band of 56°S to 61°S has no zonal boundary, where eddy activity is very strong, and the associated eastward EEF is high. Within the core of ACC, the eastward EEF (including ~50 MW/degree contribution from cyclones and

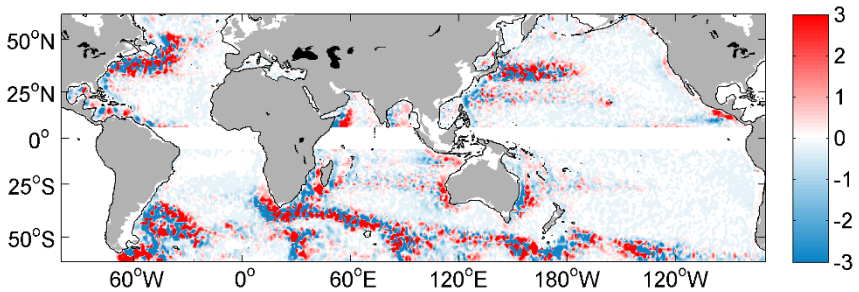

Figure 4 | The patterns of sources and sinks of eddy (with lifetimes no less than 2 weeks) energy (unit: mW/m²) derived from generation rates minus dissipation rates in 1° × 1° boxes. The interval among contours is 0.2 mW/m² and the black thin line indicates the 200-m isobath. MATLAB R2011a (http://www.mathworks.com/) with M_Map (a mapping package, http://www.eos.ubc.ca/~rich/map.html) was used to create the map.

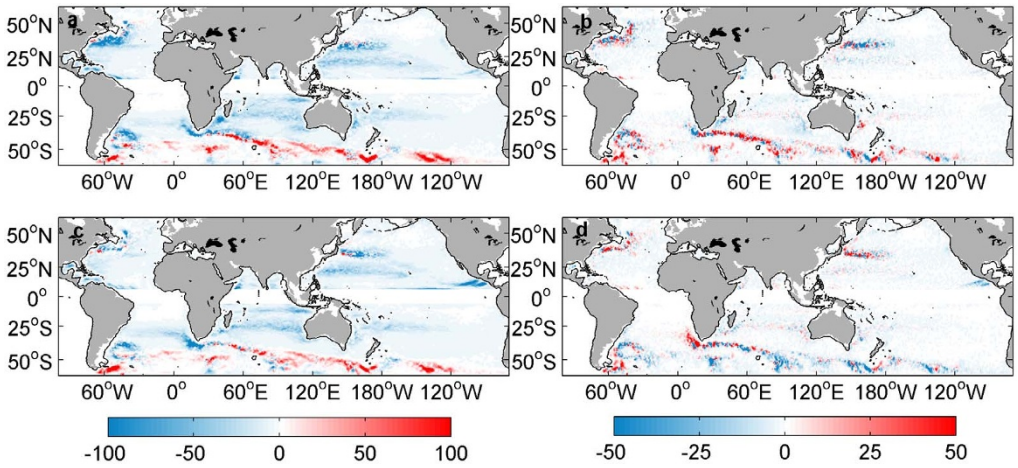

Figure 5 | The multi-years averaged zonal (a), (c) and meridional (b), (d) components of eddy-energy flux of cyclonic eddies (a), (b) and anticyclonic eddies (c), (d) with lifetimes larger than 4 weeks, in unit of MW/degree. The black thin line indicates the 200-m isobath. MATLAB R2011a (http://www.mathworks.com/) with M_Map (a mapping package, http://www.eos.ubc.ca/~rich/map.html) was used to create the map.

~50 MW/degree contribution from anticyclones) are on the order of ~100 MW/degree, with the highest value exceeding ~200 MW/degree.

Comparing with the zonal component, the meridional component of EEF does not have a clear pattern of sign in most basin interiors (Fig. 5b & 5d). Even in the subtropical bands full of eddies, there seems no well-defined sign of meridional energy transport. It seems that at a given location EKE/EAGPE transport can be either poleward or equatorward, appearing at different times. However, eddies generated in meridional boundary currents, specially the Leeuwin Current, the Agulhas Current and the Benguela Current originated from the Agulhas Retroflection, have their preferable meridional deflection according to their polarity[2,22]. Hence, there are dominant directions of meridional EKE/EAGPE transport. For example, the poleward EEF for Leeuwin Current cyclones is ~20 MW/degree, the southward energy flux of cyclones in the Agulhas Current is ~35 MW/degree, and the northward flux for Agulhas anticyclonic rings pinching off the Agulhas Retroflection and joining the Benguela Current is ~40 MW/degree. High values of meridional components of mean EEF for both cyclonic and anticyclonic eddies, are mainly concentrated in the vicinity of the major surface current systems, especially the ACC. The multi-year averaged meridional components of EEF in the ACC band are on the order of 25 MW/degree. In the ACC band meridional energy flux associated with cyclones are equatorward while those associated with anticyclones are poleward. It is opposite to what occurs north of ACC[2,22]. Such behavior is associated with the shedding process of an eastward jet, and it may be explained by the vorticity balance analysis[24].

To illustrate an overall estimate of the strength of the zonal energy transport due to eddies, the world oceans were separated into 5 zonal bands according to different eddy-concentrated regions and the meridionally-integrated zonal EEFs are shown (Fig. 6b). Nine cases of calculation based on different scales of spatial filter (with half-power cutoffs at 5°, 10° and 15°) and different thresholds of closed contour of SSHA (at ±4 cm, ±5 cm and ±6 cm) are also considered here for accuracy. Overall, there is nearly ~13.3 GW of westward eddy energy transport in the Northern Hemisphere and ~14.6 GW of westward eddy energy transport in the 5° ~ 44°S band in the

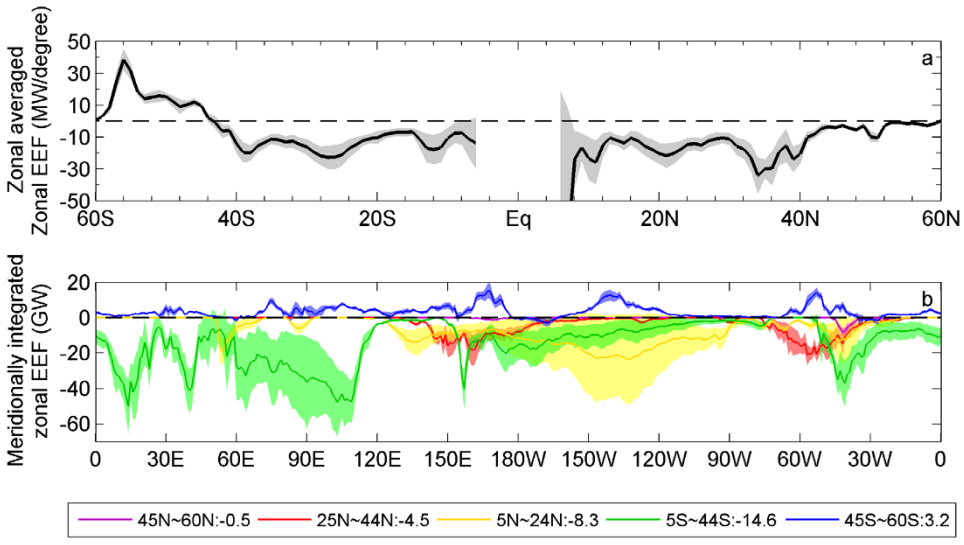

Figure 6 | Zonal and meridional distributions of zonal EEF averaged from nine cases of calculation based on different scales of spatial filter and different thresholds of closed contour of SSHA. (a), the mean zonal EEF in each 1° latitudinal band (in unit of MW/degree) with shading indicates the standard deviation over the nine cases. (b), The meridionally-integrated zonal EEF of 5 latitudinal bands (in unit of GW) with shading indicates the standard deviation over the nine cases. The numbers in the legend indicate the mean values of each solid line. MATLAB R2009a (http://www.mathworks.com/) was used to create the figure.

Southern Hemisphere. In addition, there is ~3.2 GW mean eastward eddy energy transport in the unique ACC band.

Discussion

The energy pathways (not cascade, but spatial energy flow) related to the nonlinear mesoscale eddies, the most energetic component of mesoscale variability, can be understood by connecting the energy transports with their sources and sinks. As illustrated in the Supplementary Fig. S2, the EEF vectors among different regimes of their horizontal divergence denote the energy transports between these sources and sinks on average. When westward EEFs at mid-latitudes arrive in the western boundaries, they mainly converge there, implying eddy energy dissipations dominate in the western boundaries. However, the eddy energy that dissipates here does not necessarily come from where the eddies are generated because eddy-mean flow interaction occurs everywhere during their propagation[25].

The estimates of multi-year averaged EKE/EAGPE fluxes induced by long-lived mesoscale eddies indicate that high flux of EKE/EAGPE is compatible with the locations of energetic regions of mesoscale variability. Meanwhile, it is found that the multi-year averaged EEFs result from those eddies with lifetimes no less than 17 weeks strongly contribute to the eddy energy transports in the interiors of ocean basins (Supplementary Fig. S3). More significant is that EEFs are comparable with the mean energy input from the wind into the geostrophic currents in each $1^\circ \times 1^\circ$ bin, implying most of the eddy energy, originated from potential energy of large-scale mean flow generated by the wind, is carried away by mesoscale eddies rather than dissipated locally. Thus, geostrophic eddies not only contain the most of ocean KE, but also carry and spread a significant amount of energy with them. It is noted that the EEFs estimated in this study come from mesoscale coherent vortexes, whereas a significant part of energy flux due to other types of eddying motions is not included in this estimation. Both mean advection and wind can affect the direction of EEFs, but how these effects modify EEFs is beyond the scope of this study.

There are several uncertainties in the present estimations. First, the criterion of ± 5 cm closed contour of SSHA chosen for eddy identification may underestimate the eddy area. However, the alteration of this standard does not seem to substantially affect the results. Second, a 2-dimension spatial high-pass filtering with critical half-power cutoffs was chosen and the estimates are more sensitive to the scales of spatial filter rather than the thresholds of closed contour of SSHA that were chosen in the eddy detection. Here we show spatial patterns of eddy energy, sources and sinks, and associated EEFs when spatial filter with half-power cutoffs at 10° of longitude and 10° of latitude is applied, because we confirmed that most of the eddy signals are retained from the spectrum analysis and the animations of filtered SSHA field (both not shown). Third, animation of the filtered SSHA field shows that the temporarily distorted eddies involving with eddy-flow interaction or eddy-eddy interaction in the strong currents have rather complex movements compared with the isolated eddies with persistent and coherent structures in weak flow. Thus, tracking these eddies in the ACC and WBC extensions are rather difficult, and the error of tracking results there may be relatively large. Fourth, the results reported in this paper are limited by the current state of art in this field. For example, the vertical structure of eddies is unclear. In this study, because eddies may penetrate quite deep[15–17,26–28] we use the interface depth inferred from an equivalent 2-layer model (Fig. 2 in ref. 18), which is deeper than the depth of main thermocline. The calculation is based on a working assumption that the water-column-integrated EKE is equally participated between the barotropic mode and the first baroclinic mode, and energy in higher baroclinic modes are not considered here although they are typically concentrated in the upper ocean mixed layer[29,30]. There is currently, however, no better understanding of such partition in the ocean based on observation. Thus, we adapted this seemingly crude assumption. Whether these assumptions are appropriate are left for further studies based on *in situ* observations and eddy-resolving numerical models.

Despite the potential shortcoming in these estimates, we hope that the spatial patterns of EEFs, the latitudinal variations of EEF components and other aspects of our results are useful for understanding how mesoscale eddies are transferring energy across the ocean basins.

Methods

The dataset. The weekly TOPEX/ERS merged data distributed by Archiving Validation and Interpretation of Satellite Data in Oceanography (AVISO) over period 1993 ~ 2010 were used in the analysis. They are referred to as the "Reference" Series and cover the latitude band from 60°S to 60°N on a Mercator grid with resolution of 1/3°. Through interpolation, a global dataset with uniform resolution of 1/4° by 1/4° grid was obtained. As errors of altimetry data are larger near continental boundaries, the sea surface height anomaly (SSHA) data over regimes with depth shallower than 200 meters were abandoned. Many issues related to the quality and utility of this dataset have been discussed in previous studies, e.g. refs. 2 & 3.

The stratification was calculated based on the WOA01 annual mean climatology of temperature and salinity[31]. The vertical profiles of T and S at each $1^\circ \times 1^\circ$ grid point were linearly interpolated to a vertically uniform grid of 50 meter interval. The buoyancy frequencies were calculated by using the standard Matlab subroutine: seawater (http://www.cmar.csiro.au/datacentre/ext_docs/seawater.htm).

Mesoscale eddy identification and tracking. A two-dimensional Gaussian high-pass filter was applied to the SSHA fields to identify eddy-like signals with space scales of 100 km. The filter was designed as follows:

$$K(x,y) = e^{-\frac{(x-x_0)^2+(y-y_0)^2}{2k_0^2}}, \quad (1)$$

where K is the filter transfer function and k_0 is the spatial cut-off wavelength. Here k_0 was chosen to insure that spatial filtering has half-power cutoffs at 10° of longitude and 10° of latitude; this choice of filtering retains most of mesoscale signals.

Eddy identification. Three criteria were applied to identify eddies.

1) A closed contour of SSHA $\geq \pm 5$ cm. The ± 5 cm threshold was chosen so that eddies in the relatively low-energetic and more stable regions, such as the North Pacific Subtropical Countercurrent region, are able to be detected. These eddies have shapes similar to the Gaussian profile. However closed contours in the energetic WBCs will result in larger eddy area due to higher amplitude of SSHA, and the shapes of these eddies are close to meanders. These meanders are the dominating mesoscale features drawing energy from the unstable mean flow.
2) The zonal and longitudinal spreads of the area enclosed by SSHA contour are both at least 0.5°.
3) There is at least one SSHA maximum (or minimum) in the enclosed area. To find the location of the eddy and minimize the errors, the central location of the eddy was defined as the midpoint between the centroid of the area within the closed SSHA contour and the location of the SSHA extremum. As f approaches zero near the equator, eddy calculation in this study was limited to 5° off the equator.

Eddies auto-tracking. To track nonlinear eddies at consecutive time steps, a domain as ref. 2's choice was searched. The smallest domain is a circle with radius of 150 km centralized at the center of an eddy at previous time step. A critical distance $d_c = 1.75(c_R \cdot \Delta t)$, where c_R is the local long baroclinic Rossby wave phase speed[32] and $\Delta t = 7$ days is the time step, was used. If d_c is larger than 150 km, the domain changes into an ellipse with western extremum of the distance d_c. If an eddy center at next time step is located within the searched domain derived from an eddy at the previous time step, these two eddies are considered as the same eddy at these two time steps. To avoid counting two eddies with quite different sizes at neighbor steps as one eddy, the amplitude and area of the eddy in tracking must fall within 0.25 and 2.5 times those of the reference eddy. As ref. 2 pointed out, searching ahead more than one time step is "unsuccessful"; thus, one time-step searching was used here.

EEF estimation. Eddies in the ocean are able to be classified according to their vertical structures. A common practice is based on the normal mode decomposition, i.e., observed eddies are decomposed into the barotropic mode and a seires of baroclinic modes. A critical issue is the partition of eddy energy among these possible modes. Due to the complicated nature of eddy dynamics, such a partition may depend on the time and geographic location, and it is a current research frontier.

As a working assumption, the simplified approach used in the previous study[18] is adapted in this study. Accordingly, it is assumed that the water-column-integrated kinetic energy is equally partitioned between the barotropic mode and the first baroclinic mode. Such an assumption is consistent with conclusions in previous studies that most part of KE in the upper ocean is contained in the first baroclinic mode[33] and the KE of an entire water column at periods beyond 1 day is roughly equally partitioned between the barotropic mode and the first baroclinic mode[34].

Technically, following ref. 35, an equivalent two-layer model inferred from a continuously stratified model was used, and the interfacial depth by solving the eigen value problem was shown in Fig. 2a of Ref. 18. The upper layer thickness is mostly deeper than 500 meters poleward of 40°. Within the central latitude band of ACC, especially south of 45°S, the equivalent interface depth is on the order of 1000 m. These features are respectively consistent with the climatological data analysis[26] and the model results in the subpolar gyre[27] and in the ACC band[28]. Other details of such a two-layer model are referred to ref. 18.

The total geostrophic kinetic energy of each eddy is

$$EKE = \sum_{i=1}^{n} (1-\alpha)^2 \overline{\rho} A_i (g\nabla\eta_i/f)^2 H_{1,i} H_i / H_{2,i}. \quad (2)$$

$$\alpha = \left(1 + \sqrt{\frac{H_{2,i}}{H_{1,i}} \frac{1-c}{c}}\right)^{-1}, \quad (3)$$

where $\alpha \in [0,1]$ means the fraction of the barotropic components of SSHA signals; $\overline{\rho} \simeq 1030\ kg/m^3$ is the reference density; $H_{1,i}$, $H_{2,i}$, $H_i = H_{1,i} + H_{2,i}$ are the upper-layer, lower-layer, and total thickness, respectively, at gridpoint i; c is the percentage of barotropic KE in the total EKE and assumed as 0.5; g is the gravity acceleration; η_i is SSHA at gridpoint i; A_i is area of gridbox i; n is the number of the gridpoints enclosed in the eddy boundary; $f = 2\Omega sin\theta$ is the Coriolis parameter; Ω is the earth rotation rate; and θ is the latitude.

The corresponding formula for the EAGPE is

$$EAGPE = \sum_{i=1}^{n} (1-\alpha)^2 \overline{\rho} g \eta_i^2 (H_i/H_{2,i})^2 A_i / 2\varepsilon_i, \quad (4)$$

where $\varepsilon_i = \Delta\rho_i/\overline{\rho}$ and $\Delta\rho_i$ is the density difference between the two layers at gridpoint i. How to calculate the estimates of eddy-energy dissipation/generation rates is also referred to Ref. 18.

Before the $\overrightarrow{EEF}$ is calculated, it is emphasized that the coherent mesoscale eddies identified and tracked in this paper are treated as non-dispersive structures according to Ref. 19's analysis. Thus, the phase and group velocities are not distinguished as they are for linear Rossby waves. Then, the calculation is as follows. Suppose that n eddies have passed across a meridional 1-degree line segment in the 18 years. The zonal component of the mean EEF vector there is computed as

$$EEF_{zonal} = \frac{\sum_{i=1}^{n} (E_i \frac{\Delta x_i}{\Delta l_i})}{T}, \quad (5)$$

where E_i is the total eddy energy (EKE plus EAGPE) of eddy i, Δl_i is the distance that eddy i traveled across the line segment during the time step, and Δx_i is the projection of the trajectory onto the direction-axis (so that $E\frac{\Delta x}{\Delta l}$ is the zonal component of energy flux for eddy i, and $T = 18$ years. An analogous calculation is carried out for each zonal 1-degree line segment.

1. Gould, W. J., Schmitz Jr, W. J. & Wunsch, C. Preliminary field results for a Mid-Ocean Dynamics Experiment (MODE-0). *Deep. Sea. Res.* **21**, 911–931 (1974).
2. Chelton, D. B., Schlax, M. G. & Samelson, R. M. Global observations of nonlinear mesoscale eddies. *Prog. Oceanogr.* **91**, 167–216 (2011).
3. Chelton, D. B., Schlax, M. G., Samelson, R. M. & de Szoeke, R. A. Global observations of large oceanic eddies. *Geophys. Res. Lett.* **34**, L15606 (2007).
4. Stammer, D. Global characteristics of ocean variability estimated from regional TOPEX/POSEIDON altimeter measurements. *J. Phys. Oceanogr.* **27**, 1743–1769 (1997).
5. Ducet, N., Le Traon, P. Y. & Reverdin, G. Global high-resolution mapping of ocean circulation from TOPEX/Poseidon and ERS-1 and -2. *J. Geophys. Res.* **105**, 19,477–19,498 (2000).
6. Pascual, A., Faugere, Y., Larnicol, G. & Le Traon, P. Y. Improved description of the ocean mesoscale variability by combining four satellite altimeters. *Geophys. Res. Lett.* **33**, L02611 (2006).
7. Gill, A. E., Green, J. S. A. & Simmons, A. J. Energy partition in the large-scale ocean circulation and the production of mid-ocean eddies. *Deep. Sea. Res.* **21**, 499–528 (1974).
8. Wunsch, C. The past and future ocean circulation from a contemporary perspective, in Ocean Circulation: Mechanisms and Impacts—Past and Future Changes of Meridional Overturning. *Geophys. Monogr. Ser.* **173**, 53–74 (2007).
9. Ferrari, R. & Wunsch, C. Ocean circulation kinetic energy: reservoirs, sources, and sinks. *Annu. Rev. Fluid. Mech.* **41**, 253–282 (2009).
10. Chow, C. H. & Liu, Q.-Y. Eddy effects on sea surface temperature and sea surface wind in the continental slope region of the northern South China Sea. *Geophys. Res. Lett.* **39**, L02601 (2012).
11. Waterman, S., Hogg, N. G. & Jayne, S. R. Eddy–Mean Flow Interaction in the Kuroshio Extension Region. *J. Phys.Oceanogr.* **41**, 1182–1208 (2011).
12. Polzin, K. L. Mesoscale Eddy–Internal Wave Coupling. Part II: Energetics and Results from PolyMode. *J. Phys. Oceanogr.* **40**, 789–801 (2010).
13. Elipot, S., Lumpkin, R. & Prieto, G. Modification of inertial oscillations by the mesoscale eddy field. *J. Geophys. Res.* **115**, C09010 (2010).
14. Saenko, O. A., Zhai, X., Merryfield, W. J. & Lee, W. G. The combined effect of tidally and eddy driven diapycnal mixing on the large-scale circulation. *J. Phys. Oceanogr.* **42**, 526–538 (2012).
15. Dengler, M. *et al*. Break-up of the Atlantic deep western boundary current into eddies at 8[deg] S. *Nature.* **432**, 1018–1020 (2004).
16. Lozier, M. S. Deconstructing the Conveyor Belt. *Science.* **328**, 1507–1511 (2010).
17. Adams, D. K. *et al*. Surface-Generated Mesoscale Eddies Transport Deep-Sea Products from Hydrothermal Vents. *Science.* **332**, 580–583 (2011).
18. Xu, C., Shang, X.-D. & Huang, R. X. Estimate of eddy energy generation/dissipation rate in the world ocean from altimetry data. *Ocean. Dynam.* **61**, 525–541 (2011).
19. Early, J. J., Samelson, R. M. & Chelton, D. B. The evolution and propagation of quasigeostrophic ocean eddies. *J. Phys. Oceanogr.* **41**, 1535–1555 (2011).
20. Weijer, W. *et al*. Agulhas ring formation as a barotropic instability of the retroflection. *Geophys. Res. Lett.* **40**, 5435–5438 (2013).
21. Zhai, X., Johnson, H. L. & Marshall, D. P. Significant sink of ocean-eddy energy near western boundaries. *Nat. Geosci.* **3**, 608–612 (2010).
22. Morrow, R., Birol,F., Griffin, D. & Sudre, J. Divergent pathways of cyclonic and anti-cyclonic ocean eddies. *Geophys. Res. Lett.* **31**, L24311 (2004).
23. Klocker, A. & Marshall, D. P. Advection of baroclinic eddies by depth-mean flow. *Geophys. Res. Lett.* In press (2014). DOI: 10.1002/2014GL060001.
24. Cushman-Roisin, B. & Beckers, J. Introduction to Geophysical Fluid Dynamics, Academic Press. 875 pp (2011).
25. Zu, T. *et al*. Evolution of an anticyclonic eddy southwest of Taiwan. *Ocean. Dynam.* **63**, 519–531 (2013).
26. Tulloch, R., Marshall, J., Hill, C. & Smith, K. S. Scales, Growth Rates, and Spectral Fluxes of Baroclinic Instability in the Ocean. *J. Phys. Oceanogr.* **41**, 1057–1076 (2011).
27. Zhai, X. & Marshall, D. P. Vertical Eddy Energy Fluxes in the North Atlantic Subtropical and Subpolar gyres. *J. Phys. Oceanogr.* **43**, 95–103 (2013).
28. Petersen, M. R., Willianms, S. J., Maltrud, M. E., Hecht, M. W. & Hamann, B. A three-dimensional eddy census of a high-resolution global ocean simulation. *J. Geophys. Res.* **118**, 1–16 (2013).
29. Scott, R. B. *et al*. Total kinetic energy in four global eddying ocean circulation models and over 5000 current meter records. *Ocean. Modell.* **32**, 157–169 (2010).
30. Scott, R. B. & Furnival, D. G. Assessment of Traditional and New Eigenfunction Bases Applied to Extrapolation of Surface Geostrophic Current Time Series to Below the Surface in an Idealized Primitive Equation Simulation. *J. Phys. Oceanogr.* **42**, 165–178 (2012).
31. Boyer, T. *et al*. Objective analyses of annual, seasonal, and monthly temperature and salinity for the world ocean on a 1/4 degree grid. *Int. J. Climatol.* **25**, 931–945 (2004).
32. Chelton, D. B., De Szoeke, R. A. & Schlax, M. G. Geographical variability of the first baroclinic Rossby radius of deformation. *J. Phys.Oceanogr.* **28**, 433–460 (1998).
33. Wunsch, C. The vertical partition of oceanic horizontal kinetic energy. *J. Phys.Oceanogr.* **27**, 1770–1794 (1997).
34. Ferrari, R. & Wunsch, C. The distribution of eddy kinetic and potential energies in the global ocean. *Tellus. Ser. A.* **60**, 92–108 (2010).
35. Flierl, G. R. Models of vertical structure and calibration of 2-layer models. *Dynam. Atmos. Oceans.* **2**, 341–381 (1978).

Acknowledgments

We thank Ryo Furue for his extremely careful and constructive comments on the manuscript.

This study used altimeter data available by the AVISO Altimetry Operations Center, plus hydrographic data World Ocean Atlas 2001 provided by the U.S. National Oceanographic Data Center. This study is supported by Grants XDA11010202, 2011CB403505, 2013CB430303; Projects 41306016, U1033002, 40976021 of NNSFC and LTOZZ1304. The MATLAB R2009a, R2011a were employed to plot all the figures.

Author contributions

C.X. conducted data analysis. R.X.H. and X.D.S. contributed to design of the study. C.X., X.D.S. and R.X.H. all contributed to interpretation of the results and writing of the manuscript.

Additional information

Supplementary information accompanies this paper at http://www.nature.com/scientificreports

Competing financial interests: The authors declare no competing financial interests.

How to cite this article: Xu, C., Shang, X.-D. & Huang, R.X. Horizontal eddy energy flux in the world oceans diagnosed from altimetry data. *Sci. Rep.* **4**, 5316; DOI:10.1038/srep05316 (2014).